

# Peering through the veil: accurate measurements of the Galactic nuclear star cluster

## Accurate precision photometry and extinction for the central parsec of the Galaxy

R. Schoedel<sup>1</sup>, F. Najarro<sup>2</sup>, A. Eckart<sup>3</sup>, and K. Muzic<sup>3</sup>

I. Physikalisches Institut, Universität zu Köln, Zùlpicher Strasse 77, 50937 Köln, Germany  
e-mail: eckart@ph1.uni-koeln.de

::

### ABSTRACT

*Context.* Observations of the Galactic center are biased considerably by the presence of strong and spatially highly variable interstellar extinction.

*Aims.* An accurate extinction map toward the Galactic center is essential in determining the cluster structure.

*Methods.* We use observations of the central parsec of the Milky Way that were obtained with the near-infrared camera and adaptive optics system NAOS/CONICA at the ESO VLT unit telescope 4. The field-of-view of the observations is significantly larger than the isoplanatic angle. Therefore we compare various methods of obtaining accurate photometry and astrometry in the presence of the inevitable variations of the PSF over the field.

*Results.* We present photometry in the *H* and *K*s bands for several thousands stars. An extinction map for the Galactic center is derived from these observations.

## 1. Introduction

Nuclear star clusters (NSCs) are located at the photometric and dynamical centers of almost all spiral galaxies. They have only been discovered via *HST* observations in the 1990s, but are of great interest because they are the densest and most massive clusters in their host galaxies. Frequently they contain super-massive black holes at their centers. They show signs of recurring star formation, and the discovery of rotation of the NSCs of NGC 4244 (Seth et al. 2008) and of the Milky Way (Trippe et al. 2008; Schoedel et al. 2009) indicates that NSCs may at least partially form by accretion of material from their host galaxy. A concise review of the properties of NSCs and hypotheses on their formation is given in Böker (2008).

Studying the NSC at the Galactic center (GC) is of great importance for the understanding of NSCs in general because in the next decades it will remain impossible to resolve individual stars in extragalactic NSCs (except perhaps their brightest stars), even with 50m-class telescopes. A further reason for the importance of the GC NSC is that the existence of the supermassive black hole, Sagittarius A\*, at the GC is well established and the mass of this black hole has been determined with high precision (e.g., Ghez et al. 2008; Gillessen et al. 2009).

High extinction is a serious obstacle for observational studies of the GC. Average extinction in the K-band reaches  $A_K \approx 3$ . As concerns extinction at visual wavelengths, Rieke & Lebofsky (1985) found  $A_V/A_K \sim 9$ , but more recent studies indicate higher values of  $A_V/A_K \sim 16$  (Nishiyama et al. 2008), or even  $A_V/A_K \sim 29$  (Gosling et al. 2009). Therefore, the stellar population at the GC becomes observable only at near-infrared wavelengths. Only the brightest stars can be seen in the *J*-band. Reasonable S/N on the stars is only reached in the *H*, *K*, and *L* bands. This restriction

to a tight wavelength window, where most stars show only small color indices, combined with the fact that the extinction toward the GC is not only high, but also variable on small spatial scales of a few arcseconds (Gosling et al. 2006; Schödel et al. 2007a), makes studies of the stellar population at the GC extremely difficult.

Strong interest in the stellar population at the GC was raised by spectroscopic observations, which have revealed the existence of numerous massive, young stars within 0.5 pc of Sagittarius A\*. Those young stars are witnesses of a starburst event that occurred about 4 million years ago. The young stars are arranged in a non-isotropic pattern and at least 50% of them are located in a rotating disk (Bartko et al. 2009; Lu et al. 2009, see). Although adaptive optics assisted integral field spectroscopy has resulted in the classification of hundreds of stars within  $\sim 0.5$  pc of Sagittarius A\* (Maness et al. 2007; Paumard et al. 2006, e.g.), it is extremely time consuming in both observations and data analysis. In order to efficiently probe large fields in the Galactic center for the presence of young, massive stars, it is therefore desirable to improve the photometric observations in a way that enables us to at least crudely distinguish whether a star in the GC is of early or of late spectral type. How this can be done has been demonstrated recently by (Buchholz et al. 2009). They used intermediate band filters across the K-band and used the CO bandhead absorption feature of late-type stars as a distinguishing criterion.

Accurate knowledge of extinction has impact in many different aspects of GC research: the stellar surface number density is not only a function of distance from Sagittarius A\*, but is also strongly dependent on local extinction (Schödel et al. 2007b); extinction is an important ingredient for modeling stel-

lar atmospheres (e.g., Najarro et al. 1997; Martins et al. 2007); extinction in the infrared is also important for estimating the intrinsic brightness of the near-infrared emission from the accretion flow or outflow related to Sagittarius A\* (e.g., Genzel et al. 2003; Eckart et al. 2006; Do et al. 2009). The mentioned examples show that one must know not only the value of extinction at one wavelength, but also how it changes as a function of wavelength and how it varies on spatial scales as small as one or a few arcseconds.

Until just about a decade ago, the extinction law from near- to mid-infrared wavelengths was thought to be described well by a “universal” power-law,  $A_\lambda \propto \lambda^{-\alpha}$ , with a power-law index of  $\alpha = 1.75$  (Draine 1989). First doubts on this model were shed by spectroscopic observations of the GC with ISO SWS that showed clear deviations from this model at wavelengths  $\geq 3 \mu\text{m}$  (Lutz et al. 1996). Subsequent studies have confirmed that the near- to mid-infrared extinction-law is more complex than a simple power-law. While it seems well established by now that a simple power-law is an adequate description of the wavelength dependence of extinction in the near-infrared, however with a stronger wavelength dependence as previously thought, the situation is less clear longward of  $\sim 3 \mu\text{m}$ . Nevertheless, it is clear that the extinction law decreases much less rapidly toward the mid-infrared than previously assumed. It may actually be close to constant at  $5 - 10 \mu\text{m}$ . An extensive discussion of all these points can be found in a recent publication by Nishiyama et al. (2009). In a recent study of extinction toward the nuclear bulge Gosling et al. (2009) find that the index of the power-law extinction-law can change on spatial scales as small as 5 arcseconds.

It is evident that the topic of extinction toward the central parsec of the Galaxy needs to be re-visited. Extinction maps for the central 0.5-1 pc were recently presented by Schödel et al. (2007b) and (Buchholz et al. 2009). However, these papers were not mainly focused on extinction and the extinction maps were rather side-products. Both papers used the old  $A_\lambda \propto \lambda^{-1.75}$  extinction-law (Draine 1989). Neither the extinction law nor absolute extinction were examined in depth. Also, the photometric calibration in our previous works was limited in accuracy because the PSF for the stars was either truncated (Schödel et al. 2007b) or because complex local calibration procedures had to be adopted (Buchholz et al. 2009).

Schoedel (submitted to A&A) has recently presented an easy to implement and straightforward method for the photometric analysis of AO observations with FOVs larger than the isoplanatic angle. Based on this improved method, in this paper we analyze imaging observations of the GC in the  $H$ ,  $K_s$ , and  $L'$  bands and provide accurate precision photometry for several thousand sources observed in these bands within  $\sim 1$  pc of Sagittarius A\*. We determine both the absolute extinction and the extinction law at the various bands and provide a detailed extinction map for the central parsec of the GC.

## 2. Observations

The observations used in this work were obtained with the near-infrared camera and adaptive optics (AO) system NAOS/CONICA (short NACO) at the ESO VLT unit telescope 4<sup>1</sup>. The  $\text{mag}_{K_s} \approx 6.5 - 7.0$  supergiant IRS 7 was used to close the loop of the AO, using the NIR wavefront sensor. The sky

**Table 1.** Details of the imaging observations used in this work. DIT is the detector integration time, NDIR is the number of integrations that were averaged on-line by the read-out electronics, N is the number of individually recorded exposures. The total integration time of each observation amounts to  $N \times \text{NDIT} \times \text{DIT}$ . The pixel scale of all observations is  $0.027''$  per pixel.

Date	$\lambda_{\text{central}} [\mu\text{m}]$	$\Delta\lambda [\mu\text{m}]$	N	NDIT	DIT [s]
29 April 2006	1.66	0.33	32	28	2
29 April 2006	2.18	0.35	32	28	2
26 May 2008	3.80	0.62	202	150	0.2

background was measured on a largely empty patch of sky, a dark cloud about  $400''$  north and  $713''$  east of the target. Sky subtraction, bad pixel correction, and flat fielding were applied to the individual exposures. The NACO S27 camera, with a pixel scale of  $0.027''/\text{pix}$ , was used for both  $H$  and  $K_s$  band observations. The field-of-view (FOV) of a single exposure is thus  $28'' \times 28''$ . The observations were dithered by applying a rectangular dither pattern with the center of the dithered exposures positioned approximately at  $(8.0'', -2.6'')$ ,  $(-6.1'', -2.7'')$ ,  $(-6.1'', 11.2'')$ , and  $(8.1'', 11.3'')$  east and north of Sgr A\*. In the text we refer to these four offsets as dither positions 1, 2, 3, and 4. The combined FOV of the observations is about  $40'' \times 40''$  and is offset to the north with respect to Sgr A\* because the guide star IRS 7 is located about  $5.6''$  north of Sgr A\*.

Seeing ranged between  $0.6''$  and  $1.0''$  for both  $H$  and  $K_s$  observations. Sky transparency variations were below 1% during the observations. The achieved Strehl ratio ranged between  $\sim 20\%$  ( $\sim 15\%$ ) near the guide star and  $\sim 8\%$  ( $\sim 8\%$ ) at  $25''$  distance from the guide star in the  $K_s$  ( $H$ -)band. The Strehl ratio was estimated using the *Strehl* algorithm of the ESO *eclipse* software package (Devillard 1997) on PSFs extracted at various positions in the image. From the multiple measurements we estimate the  $1\sigma$  uncertainty of the measured Strehl ratio to  $\sim 3\%$ . Table 1 summarizes the observations. The detector integration time (DIT) was set to 2.0 s in order to avoid saturation of the brightest stars. After 28 DITs, the instrument averaged the data to a single exposure (NDIT= 28). In this way, 8 individual exposures were obtained per dither position. The exposures of each respective dither position were aligned (to compensate for small residual shifts) with the *jitter* algorithm of the ESO *eclipse* software package (Devillard 1997). We show the combined FOV of the  $K_s$ -band observations in Fig. 1. Note that the photometry and astrometry in this work was done on the combined images of *each dither position* and *not on the combined mosaic* of all images (as shown in Fig. 1) in order to have a constant signal-to-noise ratio over the entire images. The  $\sim 13.5'' \times 13.5''$  overlap area between the four dither positions is indicated by the rectangle in Fig. 1.

Seeing ranged between  $1.0''$  and  $2.0''$  for the  $L'$  observations. Sky transparency variations were below 1%. The observations were random jittered, with a jitter box width of  $20''$ . Offsets by  $60''$  in random directions were alternated with observations of the target. The frames taken on the offsets frames, where the stellar density is lower, were used to construct sky frames. The 7 offset frames nearest in time to a given exposure on the target were median combined and subtracted as sky measurement. Flat fielding and bad pixel correction were applied. Finally, all exposures were combined with the *jitter* algorithm of the ESO *eclipse* software package. The resulting mosaic image is shown in Fig. 2.

<sup>1</sup> Based on observations made with ESO Telescopes at the La Silla or Paranal Observatories under programmes ID 077.B-0014 and 081.B-0648

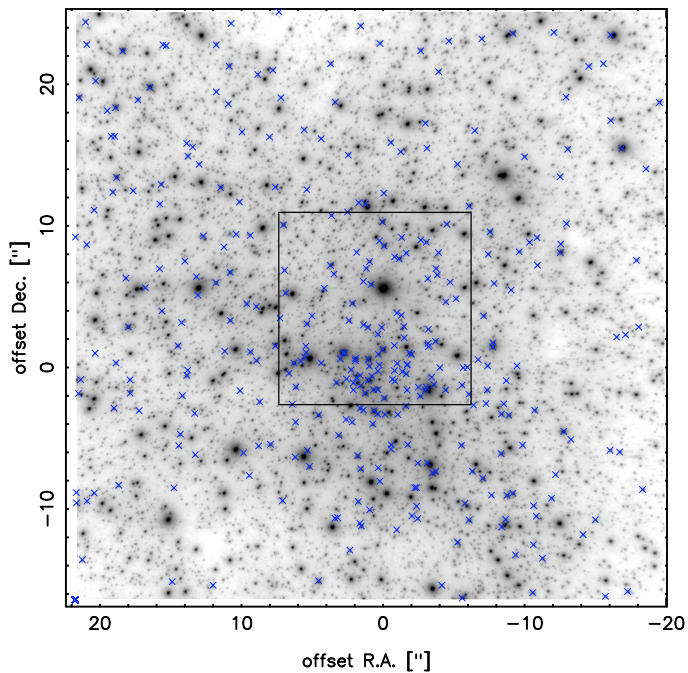


**Fig. 1.** Mosaic image of the  $Ks$ -band observations. North is up and east is to the left. Offsets are given in arcseconds from Sgr A\*. The guide star, IRS 7, is the brightest star within the rectangle, about  $5.5''$  north of Sgr A\*. The black rectangle indicates the area of overlap between the 4 dither positions. Blue crosses mark early-type stars identified by their  $H - Ks$  colors with extinction/reddening correction applied (see section 5 and Fig. 9).

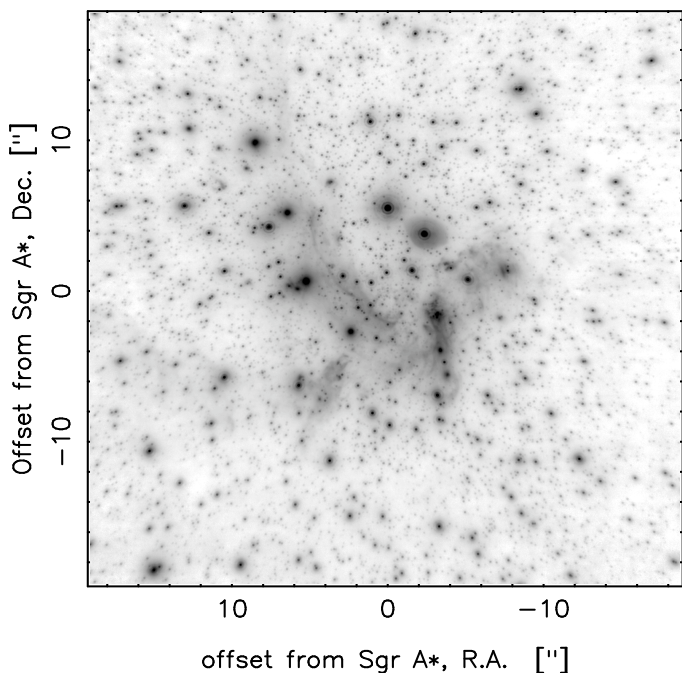


**Fig. 2.** Mosaic image of the  $Lp$ -band observations. North is up and east is to the left. Offsets are given in arcseconds from Sgr A\*.

### 3. Photometry

Due to the extreme source density at the GC aperture photometry cannot be applied accurately to GC imaging data. Therefore PSF fitting techniques must be used. In AO imaging anisoplanatic effects can lead to a systematic bias in the photometry of

point sources when PSF fitting is used for estimating the flux of the stars. This bias depends on various factors such as distance from the guide star, observing wavelength, and atmospheric conditions at the time of the observations. Various methods for dealing with anisoplanatic effects have been suggested. A straightforward and effective method to deal with anisoplanatic effects is presented in a companion paper (Schoedel, submitted to A & A). It not only provides accurate point source photometry but also reliable estimation of the diffuse background emission. In brief, the method consists of two steps: (a) linear Wiener filter deconvolution, using a point spread function (PSF) extracted from the guide star (or bright stars near the guide star), in this case IRS 7; (b) photometry and astrometry on the deconvolved image via PSF fitting with the *StarFinder* (Diolaiti et al. 2000) program package. The image is partitioned into overlapping sub-frames that are smaller than the isoplanatic angle. Those sub-frames are analyzed independently. As shown in Schoedel (2009, submitted) this method minimizes the systematic uncertainty of the photometry due to anisoplanatic effects to  $\lesssim 0.01$  mag across the  $28'' \times 28''$  FOV of the images at each dither position.

After deconvolution with PSFs extracted from IRS 7, the  $H$ - and  $Ks$ -band images from the four dither positions were partitioned into  $13 \times 13$  overlapping sub-images of  $256 \times 256$  pixel<sup>2</sup> ( $\sim 6.9'' \times 6.9''$ ). The shifts between sub-images were thus just 64 pixels in  $x$ - and/or  $y$ -direction to assure large overlap between the sub-frames. We used the following *StarFinder* parameters:  $min\_corr = 08$ ,  $thresh = [3., 3.]$ , and  $back\_box = 30$ . In order to avoid spurious detections, the process was repeated on non-deconvolved images and only sources that were discovered in both the deconvolved and non-deconvolved images were included in the final list of detected stars. The images for the diffuse background and residuals were obtained by recombining the corresponding sub-frames. The method provides two kinds of uncertainties for the photometric and astrometric measurements: *formal* uncertainties, computed by the *StarFinder* algorithm from Gaussian and photon noise, and *PSF uncertainties*, resulting from incomplete knowledge of the local PSF. The latter is calculated by comparing multiple measurements of the stars because they are present in several sub-frames (see Schoedel, submitted to A&A, for details). For stars without multiple measurements we adopted a PSF uncertainty of 0.02 mag for the  $H$ -band and 0.015 mag for the  $Ks$ -band (see Fig. 3). The results of multiple measurements were averaged. The corresponding uncertainties were calculated by quadratically combining the formal fit uncertainties with the PSF uncertainties. The data in the overlap region between the four dither positions were averaged.

Photometry on the  $L'$  image was performed in a very similar way, except that there was only one combined frame to be examined. The PSF for initial linear deconvolution was extracted from IRS 7. The size of the sub-frames for local PSF fitting was  $300 \times 300$  pixel<sup>2</sup>, with a shift of 50 pixels between the frames. Since the  $L'$  data are very rich in structure as concerns the diffuse emission, we set the *back\_box* to a smaller value (20 pixels).

Zero points for the NACO instrument for various combinations of cameras, filters, and dichroics (that split the light between wavefront sensor and camera) are determined routinely within the ESO instrument calibration plan. Zero points for all filters used in this work and for the corresponding setup (camera S27, dichroic N20C80) were determined via observation of a standard star during the same night as the observations:  $ZP_H = 23.64 \pm 0.05$ ,  $ZP_{Ks} = 22.85 \pm 0.05$ , and  $ZP_{L'} = 22.38 \pm 0.15$ .

Plots of photometric uncertainty vs. magnitude for all discovered point sources are shown in Fig. 3. The diffuse emission for all bands is shown in Fig. 4. The lists of detected point

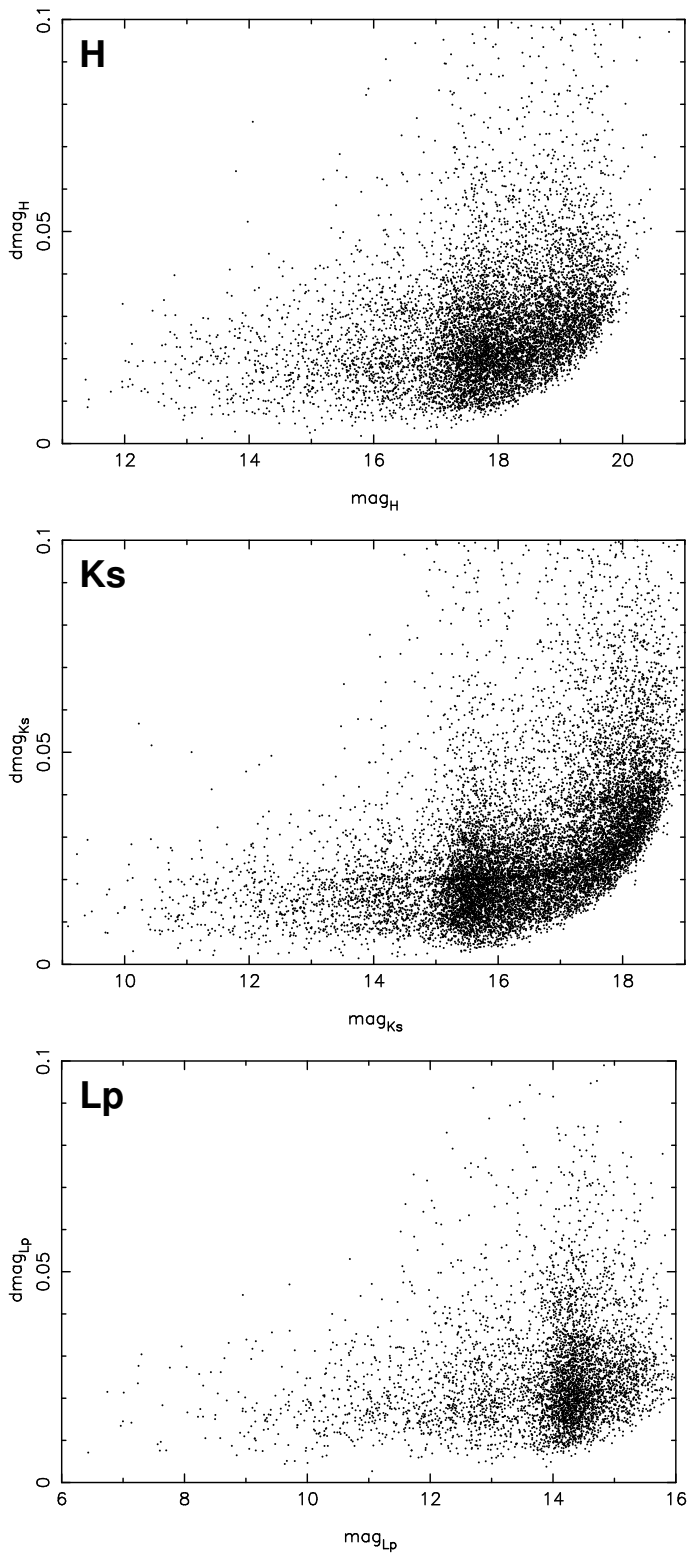


**Fig. 3.** Photometric uncertainty vs. magnitude for the  $H$ - (top),  $Ks$ - (middle), and  $L'$ - (bottom) bands.

sources in all bands were aligned with the coordinate system of the  $Ks$ -observations. The full list of detected stars and their fluxes in the different bands is given in Table A.2, available online.

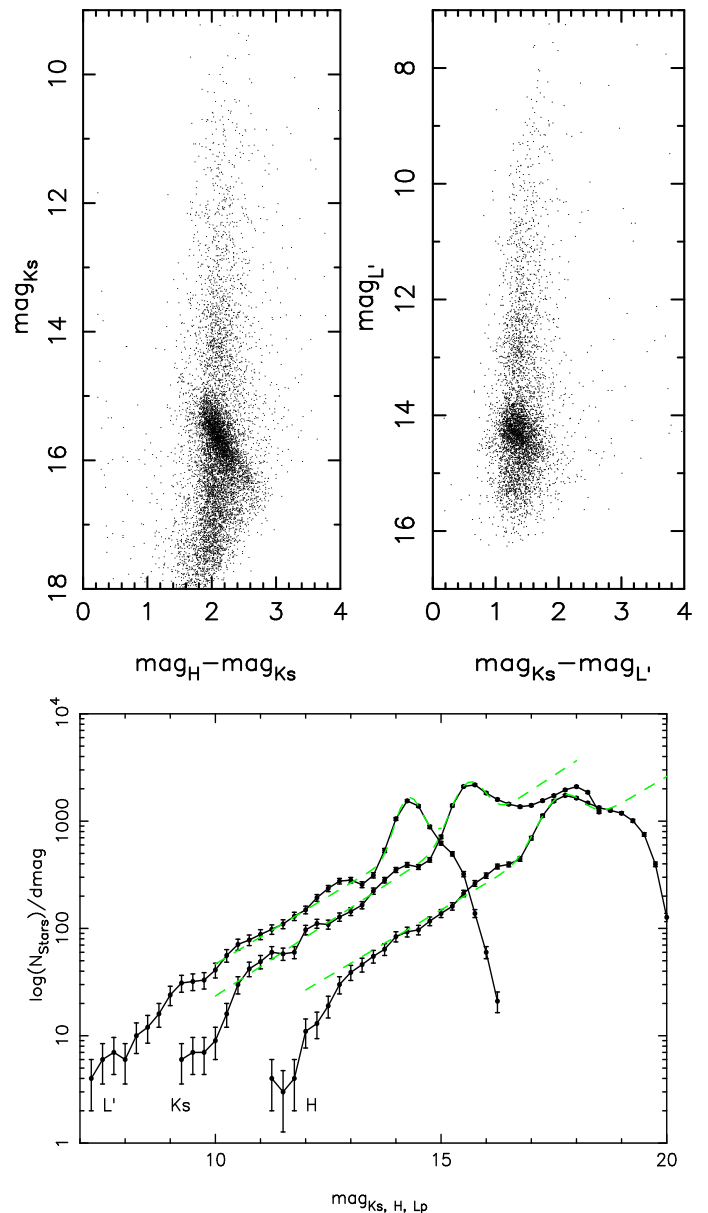


**Fig. 5.** Top: Color-magnitude diagrams; left:  $Ks$  vs.  $H - Ks$ ; right:  $L'$  vs.  $Ks - L'$ . Bottom:  $L'$ ,  $Ks$ , and  $H$  luminosity functions. The dashed green lines are fits with an exponential plus a Gaussian.

#### 4. Constraining extinction with the red clump

Color-magnitude diagrams are shown in Fig. 5. The densely populated area around  $\text{mag}_{Ks} \approx 15.5$  and  $\text{mag}_{L'} \approx 14$  is due to red clump (RC) stars, which are the equivalent to horizontal branch stars in metal-rich populations. The luminosities and colors of RC stars are narrowly distributed and are only weakly dependent on age and metallicity, particularly for clusters older than  $\sim 1.6$  Gyr (e.g., Castellani et al. 1992; Alves 2000a; Grocholski & Sarajedini 2002).

The  $H$ ,  $Ks$ , and  $L'$  luminosity functions (LFs) are shown in the bottom panel of Fig. 5. The RC feature is clearly visible as a bump in all LFs. We fitted all LFs with the combination of exponentials plus Gaussians (dashed green lines). The location of the peaks of the RC is derived from these fits as  $\text{mag}_{RC,H} = 17.71 \pm 0.01$ ,  $\text{mag}_{RC,Ks} = 15.63 \pm 0.01$ , and  $\text{mag}_{RC,L'} = 14.29 \pm 0.008$ . The uncertainties of the fits are significantly smaller than the uncertainty of the absolute photometric calibration (0.05 mag



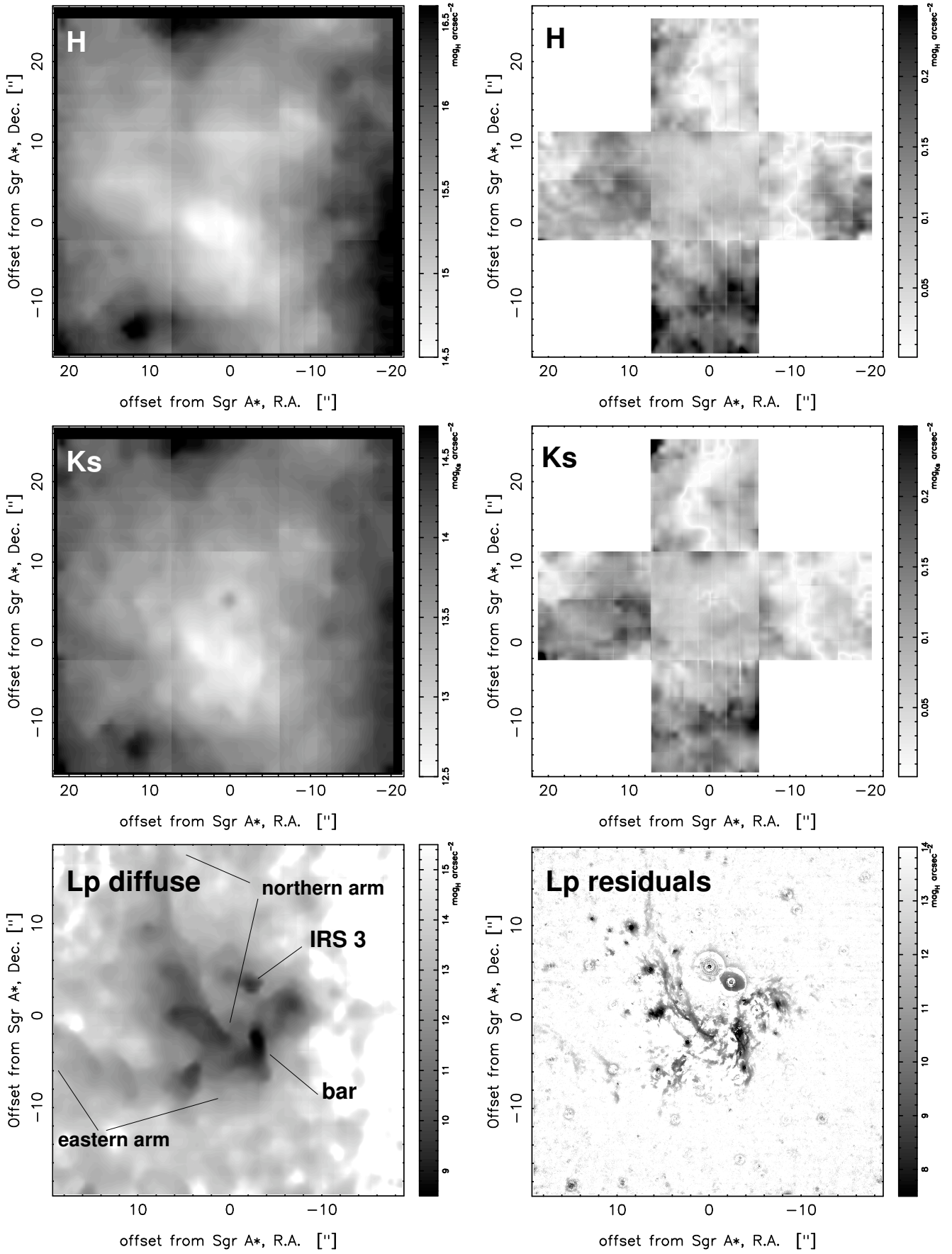


**Fig. 4.** Top to bottom left: Diffuse emission extracted from the *H*, *Ks*, and *Lp* observations. The top and middle right panels give the uncertainty of the diffuse emission, estimated from the overlap areas between the images from each of the four dither positions. The checkerboard patterns are artifacts of the image processing. The bottom right panel shows the residuals of the *Lp* image after subtraction of the point sources and of the diffuse emission.

for  $H$  and  $K_s$ , and 0.15 mag for  $L'$ ). Therefore we adopt the latter as uncertainties for the brightness of the RC in the three bands.

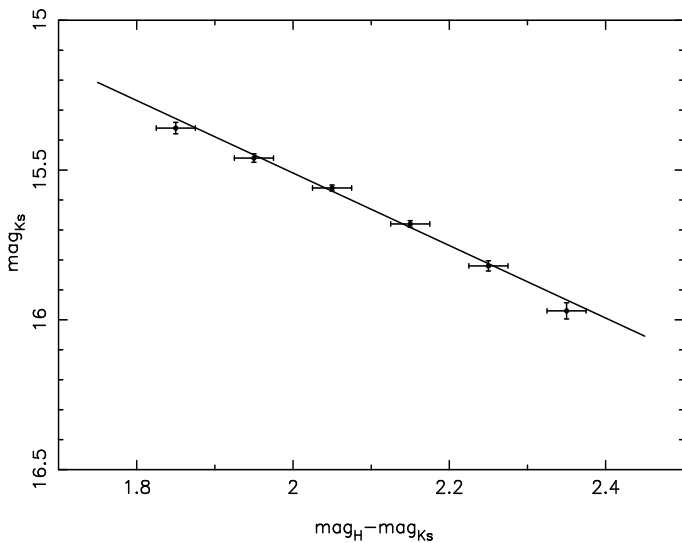


**Fig. 6.** Peak  $K_s$ -magnitude vs.  $H - K_s$  color of the red clump.

Since RC stars can be found in large numbers toward the Galactic bulge and center, they are highly useful for studying Galactic extinction and structure (e.g., Wozniak & Stanek 1996; Udalski 2003; Sumi 2004; Nishiyama et al. 2005, 2006a,b). The absolute magnitude of RC stars has been estimated to  $M_K = -1.54 \pm 0.04$  (in the 2MASS system) by Groenewegen (2008) and to  $M_K = -1.61 \pm 0.03$  by Alves (2000b). Both values are based on the *Hipparcos* catalogue. Here we adopt the more recent value for  $M_K$ . The difference between the  $K$  and  $K_s$ -magnitude is  $\approx 0.01$  mag (see discussion in Nishiyama et al. 2006b). Nishiyama et al. (2006b) estimated the distance to the GC based on photometry of RC stars, calculating the distance modulus as

$$(m - M)_0 = \text{mag}_{K_s,RC,intr.} - M_{K_s} + \Delta M_K, \quad (1)$$

where  $\text{mag}_{K_s,RC,intr.}$  is the intrinsic, reddening free magnitude of RC stars,  $M_{K_s}$  is their absolute  $K_s$ -magnitude, and  $\Delta M_K$  the population correction for  $M_{K_s}$ . We adopt the same values as Nishiyama et al. (2006b) for  $\Delta M_K = -0.07$  and use  $M_{K_s} = -1.54$  (see above). By assuming a GC distance, we can use the above equation to estimate the reddening free magnitude of RC stars. By comparing it subsequently with the magnitude of the RC clump peak as inferred from the luminosity function, we can then obtain an estimate of the absolute extinction in  $K_s$  toward the GC.

Recent estimates of the distance to the GC are  $7.52 \pm 0.36$  kpc (Nishiyama et al. 2006b),  $8.33 \pm 0.35$  kpc (Gillessen et al. 2009),  $8.0 \pm 0.6$  kpc (Ghez et al. 2008),  $7.94 \pm 0.45$  kpc (Groenewegen et al. 2008),  $8.4 \pm 0.6$  kpc (Reid et al. 2009). These distance estimates are based on different data sets and different methods and can be considered independent measurements. It appears therefore justified to combine these measurements to a weighted mean of  $R_0 = 8.0 \pm 0.2$  kpc. Using this value we obtain a reddening free magnitude of the RC bump at the GC of  $\text{mag}_{K_s,RC,intr.} = 13.04 \pm 0.10$ . All uncertainties have been quadratically combined, with the uncertainty of  $R_0$  being the dominating source of uncertainty (0.05 mag).

The fit of the RC bump in the  $K_s$ LF with a Gaussian (plus an exponential to fit the underlying luminosity function) results

in  $\text{mag}_{K_s,RC} = 15.63 \pm 0.05$ . From the difference with the theoretical reddening free magnitude of the RC bump, this results in an average extinction of  $A_{K_s} = 2.59 \pm 0.11$  toward the GC.

Assuming  $H - K_s = 0.07 \pm 0.03$  and  $K_s - L' = 0.07 \pm 0.03$  for the RC stars, we obtain in the same way estimates for  $A_H = 4.59 \pm 0.11$  and  $A_{L'} = 1.31 \pm 0.18$ . Note that these values depend only on the well-known properties of RC stars and on the GC distance. They are independent of any assumptions on the extinction-law.

Assuming the validity of a power-law for the extinction law between  $H$  and  $K_s$  and between  $K_s$  and  $L'$  (see, e.g., Nishiyama et al. 2009), we can derive the respective the power-law indices  $\alpha_{H-K_s} = 2.23 \pm 0.22$  and  $\alpha_{K_s-L'} = 1.31 \pm 0.28$ . Here the uncertainties include the uncertainties of the effective wavelengths at the corresponding bands. The effective wavelengths adopted in this work are  $\lambda_{\text{eff},H} = 1.677 \pm 0.018 \mu\text{m}$ ,  $\lambda_{\text{eff},K_s} = 2.168 \pm 0.012 \mu\text{m}$ , and  $\lambda_{\text{eff},Lp} = 3.636 \pm 0.012 \mu\text{m}$ . Details on how they have been calculated are given in appendix A.

As can be seen in Fig. 5 there is a clear dependency of the  $K_s$  peak magnitude of the RC feature on  $H - K_s$ . Because of the narrow intrinsic distribution of colors and magnitudes of the RC stars we expect this trend to be almost exclusively due to differential extinction. In order to quantify this relation, we extracted the  $K_s$ LF in narrow ranges of  $H - K_s$ . The peaks of the RC features were then fitted with a Gaussian. This method is very similar to the one applied by Nishiyama et al. (2006a), who examined the location of the RC feature in different fields toward the GC in order to derive the reddening law. The bottom panel of Fig. 6 shows the thus measured RC  $K_s$  peak magnitude vs.  $H - K_s$  along with a linear fit. Assuming  $A_\lambda \propto \lambda^{-\alpha_{H-K_s}}$ , the slope of the line gives  $\alpha_{H-K_s} = 2.36 \pm 0.13$ . As can be seen in the upper right panel of Fig. 5, there is no such clear trend of the RC visible in the plot of  $L'$  vs.  $K_s - L'$ . This is mainly because the number of stars measured in  $L'$  is smaller (smaller FOV) and because the range spanned by the  $K_s - L'$  colors is limited due to the weak extinction in  $L'$ . We can therefore not apply this method to determine  $\alpha_{K_s-L'}$  (see below for a different method, however).

## 5. An extinction map for the GC

We produced an extinction map for the FOV of the  $H$  and  $K_s$  observations of the GC by taking the median of the  $H - K_s$  colors of the 20 nearest stars at each position. Although the intrinsic colors of almost all stellar types are small at these wavelengths and therefore dominated by extinction, we tried to improve the estimates by applying a 0th order correction for intrinsic stellar colors. Stars fainter than  $\text{mag}_{K_s} = 14.5$  were assigned  $(H - K_s)_0 = 0.07$  and stars brighter than this value were assigned  $(H - K_s)_0 = 0.2$ . Known early-type stars (taken from Buchholz et al. 2009) were assigned  $(H - K_s)_0 = -0.03$ . In order to assign these intrinsic colors, we used the GC distance, extinction, and the magnitude of the stars to roughly guess their type (see, e.g., Table 3 in Buchholz et al. 2009) and assigned colors from tables 7.6 and 7.7 in Cox (2000).

The map of  $H - K_s$  colors was converted to an extinction map by assuming a power-law extinction law with an index  $\alpha_{H-K_s} = 2.23 \pm 0.32$  for the effective wavelengths of  $\lambda_H = 1.677 \pm 0.012 \mu\text{m}$  and  $\lambda_{K_s} = 2.168 \pm 0.012 \mu\text{m}$ . The uncertainty of these three parameters combined with the uncertainty of the photometric zero points results in a combined systematic uncertainty of 9.1% on the calculated values of  $A_{K_s}$ . The extinction map based on  $H - K_s$  colors is shown in the top left panel of Fig. 7. The top right panel of this figure shows the radius at each

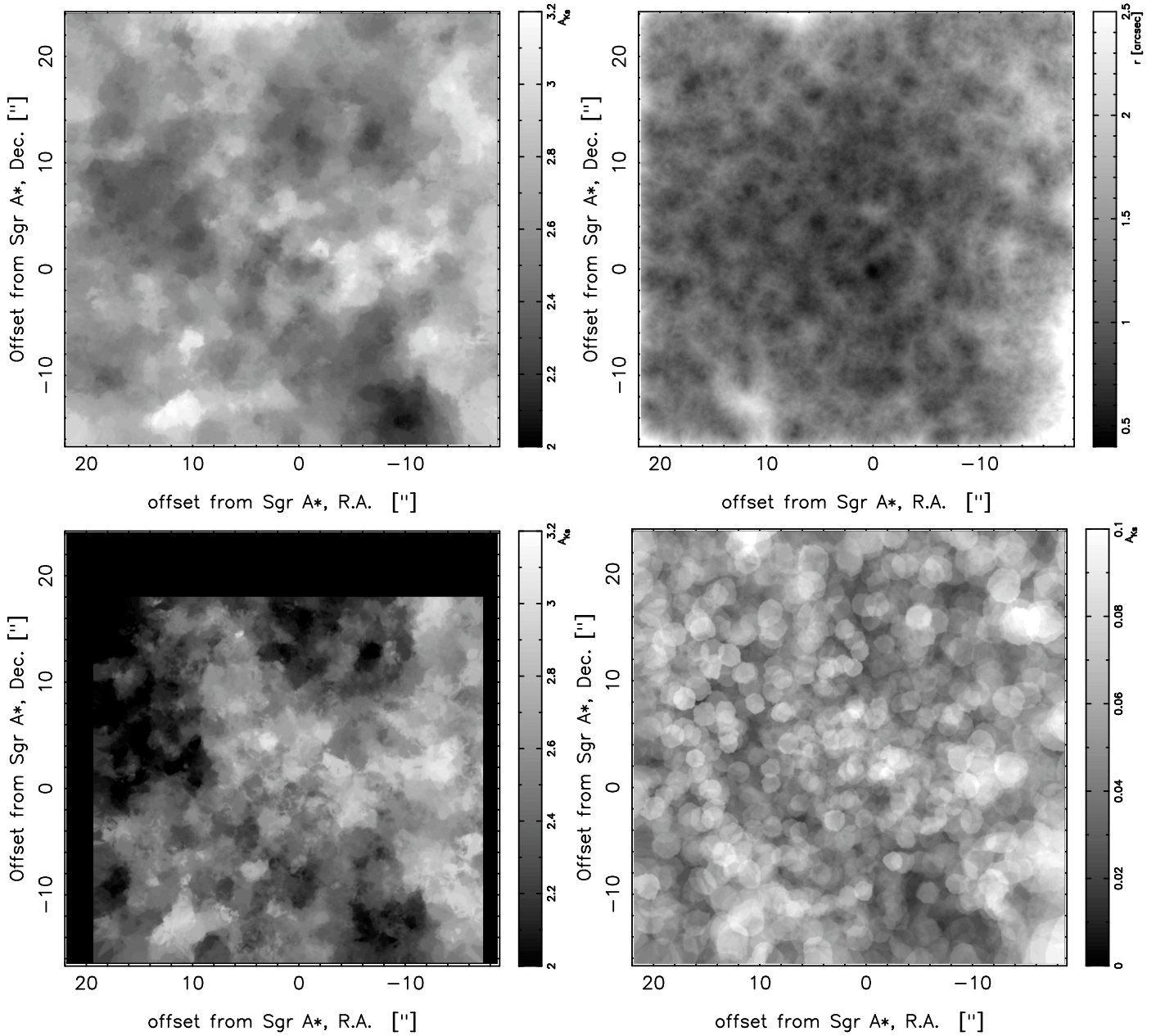


**Fig. 7.** Top left: Map of  $A_{K_s}$  for the GC derived from  $H - K_s$  colors. Top right: Map of the resolution of the extinction, i.e. the radius in arcseconds at each position within which the 20 stars for the given measurement were detected. Bottom left: Map of  $A_{K_s}$  for the GC derived from  $K_s - L'$  colors. Bottom right: Map of the statistical uncertainty of  $A_{K_s}$ , corresponding to the extinction map shown top left.

position within which 20 stars were detected, i.e. the resolution of the extinction map. The statistical uncertainty of the extinction at each point in the map is shown in the bottom right panel of Fig. 7. It is  $< 0.1$  mag for the entire map. The statistical uncertainty is somewhat correlated with the extinction because lower extinction correlates with a greater stellar density. As a cross-check, we also created an extinction map based on  $K_s - L'$  colors, in a completely analogous way. It is presented in the bottom left panel of Fig. 7 and shows the same patterns as the extinction map based on  $H - K_s$  colors. Assuming that the extinction law between  $K_s$  and  $L'$  is a power-law, we determined its index,  $\alpha_{K_s-L'}$  by requiring that the average  $A_{K_s}$  must be the same, based on  $H - K_s$  or  $K_s - L'$  colors. A value of  $\alpha_{K_s-L'} = 1.33$  has been obtained, with a statistical uncertainty of 0.13 and a systematic uncertainty – due to uncertainties in the effective wavelengths and overall photometric calibration – of 0.21.

A histogram of the measured values of  $A_{K_s}$  is shown in Fig. 8. The histogram is fit well by a Gaussian with a mean value of  $A_{K_s, \text{mean}} = 2.71$  mag and a standard deviation of 0.32 mag.

The extinction map was used to produce an extinction corrected color magnitude diagram of  $K_s$  vs.  $H - K_s$ . It is shown in Fig. 9. It can be seen how the extinction correction significantly reduces the scatter in the diagram (compare with the uncorrected diagram in Fig. 5). The red clump is very well defined and the giant sequence can be perceived clearly to the right of the dashed line, which indicates the median  $H - K_s$  color. Stars on the left of the dashed line are expected to be early-type stars. We have marked all stars with  $\text{mag}_{K_s} < 15$  and a color bluer than the median  $H - K_s$  and redder than median  $H - K_s - 0.2$  with crosses in the  $K_s$  image shown in Fig. 1. Many early-type stars reported by Paumard et al. (2006); Buchholz et al. (2009); Lu et al. (2009) and other authors are correctly identified. The

method is rather crude and we estimate that of the order 30% of the stars may be spurious identifications and a similar number of early-type stars may be missed by this method. Nevertheless, this is the first time that early-type stars at the GC are identified via broad-band imaging. Even taking into account the large estimated uncertainties, we can confirm the finding of Buchholz et al. (2009) that there are indeed early-type stars present beyond a projected radius of 0.5 pc from Sagittarius A\*.

## 6. Discussion

For comparison of the derived photometry and extinction with other work, it is important to note that such comparison is dependent on the filter system used. For example, note that the exponent used in the power-law extinction-law is strongly dependent on the effective wavelength (see, e.g., Nishiyama et al. 2006a; Gosling et al. 2009). The transmission curves of the NACO filters are available at the ESO website. In order to facilitate comparison of our work, we have calculated the effective wavelengths for the photometry presented here, using equation (A3) of Tokunaga & Vacca (2005).

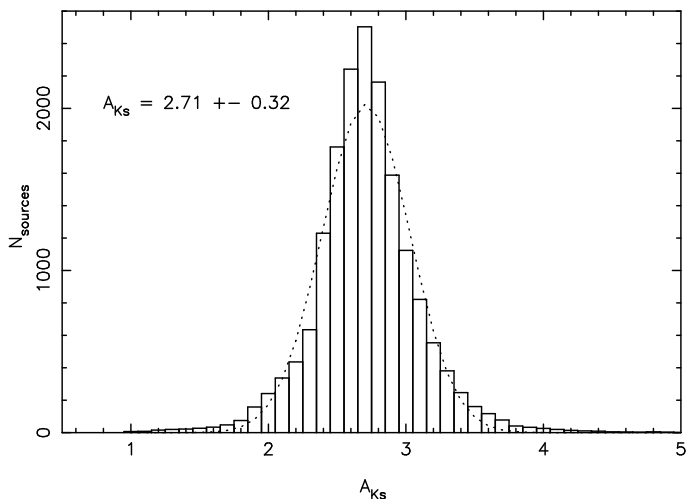


**Fig. 8.** Histogram of the extinction,  $A_{K_s}$ , based on  $H - K_s$  colors.

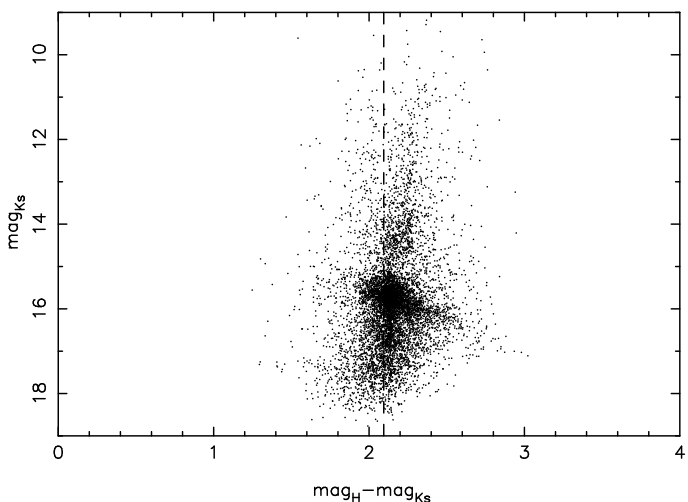


**Fig. 9.** Extinction corrected color-magnitude diagram for the GC. The dashed line indicates the mean  $H - K_s$  color.

We have found a significantly steeper extinction law at NIR wavelengths than in early work (Rieke & Lebofsky 1985; Draine 1989) on this subject. There exists, however, very good agreement between the values for  $\alpha_{H-K_s} = 2.23 \pm 0.22$  (and  $\alpha_{H-K_s} = 2.36 \pm 0.13$ , respectively) and  $\alpha_{K_s-L'} = 1.33 \pm 0.28$  found in this work and the values in other recent research. Gosling et al. (2009) report an  $\alpha_{J-K_s} = 2.64 \pm 0.52$  based on NIR observations of the nuclear bulge. Note that they find variability of this power-law index along the line-of-sight, on scales as small as 5". We have not examined spatial variability of the power-law index in our work. Since we do not have  $J$ -band observations available, we cannot determine the extinction-law toward individual stars, like the latter authors. Nishiyama et al. (2009) find  $\alpha_{H-K_s} = 2.0$  and  $\alpha_{K_s-3.6} = 1.37$  ( $\alpha_{K_s-3.6} = 1.29$ , respectively) also based on NIR observations of the Galactic nuclear bulge. Both values agree very well with our results.

The extinction map based on  $H - K_s$  colors presented in this work shows close similarity – the same features can be seen – to the one presented in Buchholz et al. (2009). The overall extinction we find in this work is, however, lower than the one reported by Buchholz et al. (2009) –  $A_{K_s} = 2.71 \pm 0.32$  compared to  $A_{K_s} = 3.14 \pm 0.43$ . The reason for this difference is the assumption of a flatter extinction law (based on Draine 1989) in Buchholz et al. (2009). The extinction map presented by Schödel et al. (2007b) is also similar to the one presented here, but shows a smaller FOV and is also based on a different extinction law.

## 7. Summary

We provide accurate and precise photometry for several thousand point sources extracted from adaptive optics observations of the central parsec of the Galactic center in the  $H$ ,  $K_s$ , and  $L'$  bands. The data are made publicly available. Adaptive optics photometry has been published previously in some papers. However, we believe that those earlier results are only of limited general use or are complementary to this data set because of reasons such as: (a) limited field-of-view of previous observations or focus on the central few 0.1 pc; (b) isoplanatic effects were not taken properly into account; (c) bias by the application of methods such as Lucy-Richardson deconvolution; (d) no transparent explanation of the photometric calibration. This data set is the most comprehensive one published so far.

Based on the photometric results, we analyze extinction toward the central parsec of the GC. Absolute values of extinction in the three examined bands are derived based on the well-known properties of red clump stars, without the need to measure stellar colors and without having to assume an extinction law. The values obtained are  $A_H = 4.59 \pm 0.11$  mag,  $A_{K_s} = 2.59 \pm 0.11$  mag, and  $A_{L'} = 1.31 \pm 0.28$  mag. This results in  $A_H : A_{K_s} : A_{L'} = 1.77 : 1 : 0.51$ . Assuming the validity of a power-law extinction law between  $H$  and  $K_s$  and between  $K_s$  and  $L'$ , this is equivalent to power-law indices of  $\alpha_{H-K_s} = 2.23 \pm 0.22$  and  $\alpha_{K_s-L'} = 1.31 \pm 0.28$ . This is significantly steeper than in earlier work (e.g. Rieke & Lebofsky 1985; Draine 1989), but agrees with recent studies of extinction toward the nuclear bulge (Nishiyama et al. 2009; Gosling et al. 2009). We also confirm the flattening of the extinction law beyond  $\sim 3 \mu\text{m}$  (see also Lutz et al. 1996; Indebetouw et al. 2005; Viehmann et al. 2005; Flaherty et al. 2007; Nishiyama et al. 2009).

Based on  $H - K_s$  colors of the stars, we provide a detailed, accurate extinction map for a FOV of  $40'' \times 40''$  ( $\sim 1.5 \text{ pc} \times 1.5 \text{ pc}$ ) centered roughly on Sagittarius A\*. The spatial resolution of the map is  $\sim 1''$ . Both statistical and systematic uncertainties of the extinction map are lower than 10%. Extinction varies signifi-



cantly on arcsecond scales. The mean extinction based on stellar colors is found to be  $A_{K_s} = 2.71 \pm 0.32$  mag, in good agreement with the value of mean extinction based on the RC method. An extinction map based on  $K_s - L'$  colors, although less accurate because of lower source numbers and possible stronger contamination by diffuse emission from dust, confirms the patterns seen in the extinction map based on  $H - K_s$  colors. Requiring the mean extinction between the two maps to be the same, we derive  $\alpha_{K_s-L'} = 1.33 \pm 0.25$ , in excellent agreement with the value of this parameter derived from the mean magnitudes of the RC bump (see above).

Applying the derived extinction law and the measured absolute extinction to the observed  $H - K_s$  colors of the stars, we are able to correct the corresponding color-magnitude diagram. This reduces the scatter in this diagram considerably and makes it possible, for the first time, to clearly distinguish the giant branch and the main sequence branch in such a diagram for the GC.

*Acknowledgements.* RS acknowledges the Ramón y Cajal programme of the Spanish Ministerio de Ciencia e Innovación.

## References

- Alves, D. R. 2000a, *ApJ*, 539, 732  
 Alves, D. R. 2000b, *ApJ*, 539, 732  
 Bartko, H., Martins, F., Fritz, T. K., et al. 2009, *ApJ*, 697, 1741  
 Böker, T. 2008, *Journal of Physics Conference Series*, 131, 012043  
 Buchholz, R. M., Schödel, R., & Eckart, A. 2009, *ArXiv e-prints*, 499, 483  
 Castellani, V., Chieffi, A., & Straniero, O. 1992, *ApJS*, 78, 517  
 Cox, A. N. 2000, *Allen's astrophysical quantities*, ed. A. N. Cox  
 Devillard, N. 1997, *The Messenger*, 87, 19  
 Diolaiti, E., Bendinelli, O., Bonaccini, D., et al. 2000, in *Society of Photo-Optical Instrumentation Engineers (SPIE) Conference Series*, Vol. 4007, Society of Photo-Optical Instrumentation Engineers (SPIE) Conference Series, ed. P. L. Wizinowich, 879–888  
 Do, T., Ghez, A. M., Morris, M. R., et al. 2009, *ApJ*, 691, 1021  
 Draine, B. T. 1989, in *ESA Special Publication*, Vol. 290, *Infrared Spectroscopy in Astronomy*, ed. E. Böhm-Vitense, 93–98  
 Eckart, A., Baganoff, F. K., Schödel, R., et al. 2006, *A&A*, 450, 535  
 Flaherty, K. M., Pipher, J. L., Megeath, S. T., et al. 2007, *ApJ*, 663, 1069  
 Genzel, R., Schödel, R., Ott, T., et al. 2003, *Nature*, 425, 934  
 Ghez, A. M., Salim, S., Weinberg, N. N., et al. 2008, *ApJ*, 689, 1044  
 Gillessen, S., Eisenhauer, F., Trippe, S., et al. 2009, *ApJ*, 692, 1075  
 Gosling, A. J., Bandyopadhyay, R. M., & Blundell, K. M. 2009, *MNRAS*, 394, 2247  
 Gosling, A. J., Blundell, K. M., & Bandyopadhyay, R. 2006, *ApJ*, 640, L171  
 Grocholski, A. J. & Sarajedini, A. 2002, *AJ*, 123, 1603  
 Groenewegen, M. A. T. 2008, *A&A*, 488, 935  
 Groenewegen, M. A. T., Udalski, A., & Bono, G. 2008, *A&A*, 481, 441  
 Indebetouw, R., Mathis, J. S., Babler, B. L., et al. 2005, *ApJ*, 619, 931  
 Lord, S. 1992, *Tech. rep.*  
 Lu, J. R., Ghez, A. M., Hornstein, S. D., et al. 2009, *ApJ*, 690, 1463  
 Lutz, D., Feuchtgruber, H., Genzel, R., et al. 1996, *A&A*, 315, L269  
 Maness, H., Martins, F., Trippe, S., et al. 2007, *ApJ*, 669, 1024  
 Martins, F., Genzel, R., Hillier, D. J., et al. 2007, *A&A*, 468, 233  
 Najarro, F., Krabbe, A., Genzel, R., et al. 1997, *A&A*, 325, 700  
 Nishiyama, S., Nagata, T., Baba, D., et al. 2005, *ApJ*, 621, L105  
 Nishiyama, S., Nagata, T., Kusakabe, N., et al. 2006a, *ApJ*, 638, 839  
 Nishiyama, S., Nagata, T., Sato, S., et al. 2006b, *ApJ*, 647, 1093  
 Nishiyama, S., Nagata, T., Tamura, M., et al. 2008, *ApJ*, 680, 1174  
 Nishiyama, S., Tamura, M., Hatano, H., et al. 2009, *ApJ*, 696, 1407  
 Paumard, T., Genzel, R., Martins, F., et al. 2006, *ApJ*, 643, 1011  
 Reid, M. J., Menten, K. M., Zheng, X. W., et al. 2009, *ArXiv e-prints*  
 Rieke, G. H. & Lebofsky, M. J. 1985, *ApJ*, 288, 618  
 Schödel, R., Eckart, A., Alexander, T., et al. 2007a, *A&A*, 469, 125  
 Schödel, R., Eckart, A., Alexander, T., et al. 2007b, *A&A*, 469, 125  
 Schoedel, R., Merritt, D., & Eckart, A. 2009, *ArXiv e-prints*  
 Seth, A. C., Blum, R. D., Bastian, N., Caldwell, N., & Debattista, V. P. 2008, *ApJ*, 687, 997  
 Sumi, T. 2004, *MNRAS*, 349, 193  
 Tokunaga, A. T. & Vacca, W. D. 2005, *PASP*, 117, 421  
 Trippe, S., Gillessen, S., Gerhard, O. E., et al. 2008, *A&A*, 492, 419  
 Udalski, A. 2003, *ApJ*, 590, 284  
 Viehmann, T., Eckart, A., Schödel, R., et al. 2005, *A&A*, 433, 117  
 Wozniak, P. R. & Stanek, K. Z. 1996, *ApJ*, 464, 233

## Appendix A: Effective wavelength

We calculated the effective wavelengths of our observations following equation (A3) of Tokunaga & Vacca (2005). The transmission curves for the NACO  $H$  and  $K_s$  filters were downloaded from the instrument web site<sup>2</sup>. Spectra of the atmospheric transmission were downloaded from the Gemini telescope web site<sup>3</sup>. They are based on models with the ATRAN software (Lord 1992). The transmission curves for 3 mm precipitable water vapor were used because humidity was high during the  $H$  and  $K_s$  observations.

We did not use any particular stellar atmosphere model for the calculations. Instead, simple extinguished blackbody models were used. Table A.1 lists the values of the effective wavelength for various values of  $A_K$  and effective temperatures of the blackbodies. A power-law  $A_K \propto \lambda^{-\alpha}$  (Nishiyama et al. 2009) was used to calculate the extinction at different wavelengths. We assumed  $\alpha_{H-K_s} = 2.23$  for the extinction between  $H$  and  $K_s$ , and  $\alpha_{K_s-L'} = 1.33$  for the extinction between  $K_s$  and  $L'$ . The majority (> 90%) of stars in the images analyzed in this work are of late-type, with a large percentage of RC stars (see, e.g., Buchholz et al. 2009). We therefore adopt as effective wavelengths  $\lambda_{\text{eff},H} = 1.677 \mu\text{m}$ ,  $\lambda_{\text{eff},K_s} = 2.168 \mu\text{m}$ , and  $\lambda_{\text{eff},L'} = 3.636 \mu\text{m}$  for an average extinction of  $A_{K_s} \approx 2.5$ .

The uncertainty introduced by the choice for the amount of precipitable water vapor is low. Choosing 1.6 mm instead of 3.0 mm will change the effective wavelengths by  $\leq 0.003$  for  $H$ ,  $\leq 0.001$  for  $K_s$ , and  $\leq 0.01$  for  $L'$ . Changing the power-law index for the extinction curve between  $H$  and  $K_s$  to  $\alpha_{H-K_s} = 2.0$  (Nishiyama et al. 2009) results in a change of  $\leq 0.003 \mu\text{m}$  for  $\lambda_{\text{eff},K_s}$ , and  $\leq 0.009 \mu\text{m}$  for  $\lambda_{\text{eff},H}$ . Changing the power-law index for the extinction curve between  $K_s$  and  $L'$  to  $\alpha_{K_s-L'} = 1.37$  (Nishiyama et al. 2009) results in a change of  $< 0.001 \mu\text{m}$  for  $\lambda_{\text{eff},L'}$ . The uncertainty in extinction introduces an uncertainty of  $\lesssim 0.015 \mu\text{m}$  for  $H$ ,  $\lesssim 0.01 \mu\text{m}$  for  $K_s$ , and  $\lesssim 0.002 \mu\text{m}$  for  $L'$ . The unknown effective temperature of the stars introduces uncertainties of  $\lesssim 0.005 \mu\text{m}$  for  $H$ ,  $\lesssim 0.006 \mu\text{m}$  for  $K_s$ , and  $\lesssim 0.001 \mu\text{m}$  for  $L'$ .

We estimate the combined  $1 \sigma$  uncertainty of the effective wavelengths to  $0.018 \mu\text{m}$  for  $H$ ,  $0.012 \mu\text{m}$  for  $K_s$ , and  $0.012 \mu\text{m}$  for  $L'$ .

<sup>2</sup> <http://www.eso.org/sci/facilities/paranal/instruments/naco/index.html>

<sup>3</sup> <http://www.gemini.edu/node/10781?q=node/10789>

**Table A.1.** Effective wavelengths for the NACO  $H$ ,  $K_s$ , and  $L'$  filters for blackbodies with different effective temperatures and extinction. The effective temperature is given in the left column, the extinction  $A_{K_s}$  in the first line of the two tables.

$H$	2.0	2.5	3.0	3.5
3000	1.674	1.681	1.688	1.695
4700	1.669	1.677	1.684	1.691
30000	1.664	1.672	1.680	1.687
$K_s$				
3000	2.167	2.171	2.176	2.180
4700	2.163	2.168	2.173	2.177
30000	2.159	2.164	2.169	2.174
$L'$				
3000	3.636	3.637	3.638	3.639
4700	3.635	3.636	3.637	3.638
30000	3.634	3.635	3.636	3.637

**Table A.2.** List of detected point sources in the  $H$ ,  $K_s$ , and  $L'$ -band observations. Coordinates are given as offsets from Sgr A\*. Uncertainties in the astrometric positions can be as large as  $\sim 0.1''$  because high precision astrometry was not at the focus of this work. The conversion to offsets from Sgr A\* was done by assuming a pixel scale of  $0.027''$  per pixel (ESO NACO manual). The camera rotation angle was assumed 0 deg east of north and no camera distortion solution was applied. The second column gives the projected distance from Sgr A\* in arcseconds. We only include the first ten lines of the table in the printed edition of this work. The photometric uncertainties include formal uncertainties from PSF fitting, based on Gaussian read-out noise and Poisson photon noise, and the uncertainties due to the limited knowledge of the PSF. The  $1\sigma$  uncertainties of the zero points are not included. They are  $\Delta ZP_H = 0.05$ ,  $\Delta ZP_{K_s} = 0.05$ , and  $\Delta ZP_{L_p} = 0.15$ .

ID	$R_{\text{SgrA}^*}$ [ $''$ ]	R.A. [ $''$ ]	Dec. [ $''$ ]	mag $_H$	$\Delta\text{mag}_H$	mag $_{K_s}$	$\Delta\text{mag}_{K_s}$	mag $_{L_p}$	$\Delta\text{mag}_{L_p}$
1	0.048	0.007	-0.048	17.53	0.05	15.67	0.02	0	0
2	0.056	0.016	-0.053	17.52	0.15	15.52	0.02	0	0
3	0.098	-0.079	0.059	18.77	0.09	16.91	0.02	0	0
4	0.112	0.03	-0.108	18.09	0.04	16.39	0.16	0	0
5	0.139	0.139	0.009	0	0	17.5	0.02	0	0
6	0.146	-0.129	0.067	0	0	17.06	0.03	0	0
7	0.161	-0.007	0.161	16.15	0.15	14.19	0.06	12.98	0.02
8	0.232	0.19	0.133	16.99	0.02	15.1	0.02	0	0
9	0.245	-0.23	-0.085	18.74	0.04	16.96	0.1	0	0
10	0.268	0.023	-0.267	16.66	0.02	14.79	0.03	0	0